The Astrophysical Journal Letters, 947:L11 (11pp), 2023 April 10 https://doi.org/10.3847/2041-8213/acc84b

Synchrotron Radiation Dominates the Extremely Bright GRB 221009A

Jun Yang[1,2], Xiao-Hong Zhao[3,4,5], Zhenyu Yan[1,2], Xiangyu Ivy Wang[1,2], Yan-Qiu Zhang[6,7], Zheng-Hua An[6], Ce Cai[8], Xin-Qiao Li[6], Zihan Li[1], Jia-Cong Liu[6,7], Zi-Ke Liu[1,2], Xiang Ma[6], Yan-Zhi Meng[1,2], Wen-Xi Peng[6], Rui Qiao[6], Lang Shao[9], Li-Ming Song[6], Wen-Jun Tan[6,7], Ping Wang[6], Chen-Wei Wang[6,7], Xiang-Yang Wen[6], Shuo Xiao[10], Wang-Chen Xue[6,7], Yu-Han Yang[11], Yi-Han Iris Yin[12], Bing Zhang[13], Fan Zhang[6], Shuai Zhang[9], Shuang-Nan Zhang[6], Chao Zheng[6,7], Shi-Jie Zheng[6], Shao-Lin Xiong[6], and Bin-Bin Zhang[1,2,14]

[1] School of Astronomy and Space Science, Nanjing University, Nanjing 210093, People's Republic of China
[2] Key Laboratory of Modern Astronomy and Astrophysics (Nanjing University), Ministry of Education, People's Republic of China
[3] Yunnan Observatories, Chinese Academy of Sciences, Kunming, People's Republic of China; zhaoxh@ynao.ac.cn
[4] Center for Astronomical Mega-Science, Chinese Academy of Sciences, Beijing, People's Republic of China
[5] Key Laboratory for the Structure and Evolution of Celestial Objects, Chinese Academy of Sciences, Kunming, People's Republic of China
[6] Key Laboratory of Particle Astrophysics, Institute of High Energy Physics, Chinese Academy of Sciences, 19B Yuquan Road, Beijing 100049, People'S Republic Of China; xiongsl@ihep.ac.cn
[7] University of Chinese Academy of Sciences, Beijing 100049, People's Republic of China
[8] College of Physics and Hebei Key Laboratory of Photophysics Research and Application, Hebei Normal University, Shijiazhuang, Hebei 050024, People's Republic of China
[9] College of Physics, Hebei Normal University, Shijiazhuang 050024, People's Republic of China
[10] Guizhou Provincial Key Laboratory of Radio Astronomy and Data Processing, Guizhou Normal University, Guiyang 550001, People'S Republic Of China
[11] Department of Physics, University of Rome "Tor Vergata", via della Ricerca Scientifica 1, I-00133 Rome, Italy
[12] School of Physics, Nanjing University, Nanjing 210093, People's Republic of China
[13] Department of Physics and Astronomy, University of Nevada Las Vegas, NV 89154, USA; bbzhang@nju.edu.cn
[14] Purple Mountain Observatory, Chinese Academy of Sciences, Nanjing 210023, People's Republic of China
Received 2023 March 1; revised 2023 March 21; accepted 2023 March 27; published 2023 April 14

Abstract

The brightest gamma-ray burst, GRB 221009A, has spurred numerous theoretical investigations, with particular attention paid to the origins of ultrahigh-energy TeV photons during the prompt phase. However, analyzing the mechanism of radiation of photons in the ∼MeV range has been difficult because the high flux causes pileup and saturation effects in most GRB detectors. In this Letter, we present systematic modeling of the time-resolved spectra of the GRB using unsaturated data obtained from the Fermi Gamma-ray Burst Monitor (precursor) and SATech-01/GECAM-C (main emission and flare). Our approach incorporates the synchrotron radiation model, which assumes an expanding emission region with relativistic speed and a global magnetic field that decays with radius, and successfully fits such a model to the observational data. Our results indicate that the spectra of the burst are fully in accordance with a synchrotron origin from relativistic electrons accelerated at a large emission radius. The lack of thermal emission in the prompt emission spectra supports a Poynting flux–dominated jet composition.

Unified Astronomy Thesaurus concepts: Gamma-ray bursts (629)

1. Introduction

Despite extensive research spanning several decades, the radiation mechanism of gamma-ray bursts (GRBs) in the prompt phase still remains elusive (see Kumar & Zhang 2015; Zhang 2018 for reviews). A typical GRB spectrum can be empirically described as a broken power-law function, namely, the so-called Band function (Band et al. 1993). The low- and high-energy slopes are typically $\alpha \sim -1$ and $\beta \sim -2.2$ (Preece et al. 2000; Kaneko et al. 2006), respectively. The prevalence of nonthermal spectra in GRBs indicates that photosphere emission (Mészáros & Rees 2000; Rees & Mészáros 2005; Lazzati & Begelman 2010; Beloborodov 2010) is unlikely to be the dominant mechanism. Instead, synchrotron radiation (Daigne & Mochkovitch 1998; Ghisellini et al. 2000; Daigne et al. 2011; Burgess et al. 2014, 2020; Zhang 2020; Wang et al. 2022) appears to be the most favorable explanation for most GRB spectra. The synchrotron origin of prompt emission is also supported by broadband data spanning a wide range of wavelengths, from gamma rays down to the optical band (Oganesyan et al. 2017, 2018; Ravasio et al. 2018; Oganesyan et al. 2019; Ravasio et al. 2019).

However, the measured low energy slope of $\alpha \sim -1$ contradicts the simplest synchrotron model, which assumes a constant magnetic field. Uhm & Zhang (2014) argued that if the GRB emission comes from electrons emitting in a large radius from the central engine, as is the case for models invoking magnetic dissipation in a Poynting flux–dominated jet (e.g., Zhang & Yan 2011), the magnetic field strength would decay as a function of time as the emitter moves to larger distances. Such a model can account for a typical Band spectrum and interpret the GRB data well, as has been shown in direct comparisons between the model and GRB data (Zhang et al. 2016, 2018). Nevertheless, it is in general challenging to compare the models with observational data, as it necessitates the use of bright GRBs to obtain finely resolved time-dependent spectra.

GRB 221009A, which was observed recently on 2022 October 9, at 13:16:59.99 Coordinated Universal Time (hereafter T_0), is notable for being the most luminous and energetic GRB ever recorded, owing to its exceptional isotropic-equivalent energy output of approximately 10^{55} erg (see also

An et al. 2023) and its relatively close distance at a redshift of $z = 0.151$ (Castro-Tirado et al. 2022; Malesani et al. 2023). Furthermore, the detection of ultrahigh-energy TeV photons associated with this event (Huang et al. 2022) has sparked intense debate regarding their origin, encompassing discussions on whether they arise from internal dissipation or external shock and whether they originate from the leptonic or hadronic process (Ren et al. 2022; Alves Batista 2022; Zhang et al. 2022; Sato et al. 2022; Rudolph et al. 2023; Wang et al. 2023).

GRB 221009A triggered several high-energy missions, including the Gamma-ray Burst Monitor (GBM; Meegan et al. 2009) on board The Fermi Gamma-Ray Space Telescope (Veres et al. 2022) and GECAM-C on board The SATech-01 Satellite (Liu et al. 2022). However, its extraordinary brightness led to some irreparable effects on the data of most detectors, such as data saturation and pulse pileup. Nevertheless, we were able to accurately capture the full temporal profile and obtain high-time-resolution spectra by combining data from Fermi/GBM and SATech-01/GECAM-C during the prompt emission.

Figure 1 demonstrates that the prompt emission phase of GRB 221009A lasts around 600 s after T_0 and can be segmented into three distinct episodes. The first episode is considered a precursor emission of the burst, which exhibits a fast-rising exponential-decay (FRED) shape and lasts for about 30 s. After a quiet period of 180 s, the main emission episode appears from 220 to 270 s and features two consecutive pulses dominating its temporal profile. Finally, the flare episode takes over, with the majority of its emission concentrated between 500 and 520 s. The exceptional intensity of all three episodes presents a unique opportunity to validate the synchrotron model through the use of time-resolved spectral data. In this Letter, we first conducted a thorough analysis of the observational data by Fermi/GBM and SATech-01/GECAM-C (Section 2). We then expounded on the physical framework of our model in Section 3. The fitting procedures were thoroughly outlined in Section 4, and the subsequent results and implications were discussed in Section 5.

2. Data Reduction and Analysis

Analyzing the prompt emission of GRB 221009A has been demonstrated to be a challenging task due to its exceptional brightness posing significant electronic disturbances for the majority of GRB detectors, inducing but not limited to data saturation and pulse pileup effects (e.g., Frederiks et al. 2023). Fortunately, the moderately bright precursor episode can be accurately recorded by sensitive gamma-ray detectors, such as the Fermi/GBM, without suffering from the abovementioned effects (Lesage et al. 2022). During the main emission and flare episodes, the GRD01 detector of the SATech-01/GECAM-C, thanks to its specialized design and special working mode, was confirmed to be capable of avoiding data saturation and pulse pileup issues, and hence recording precise light curves and spectral shapes (Liu et al. 2022). Therefore, we combine the Fermi/GBM data from the precursor episode with the SATech-01/GECAM-C data from the main emission and flare episodes and attempt to explain the complete prompt emission of GRB 221009A using the synchrotron radiation model.

The procedure for data reduction and analysis of Fermi/GBM data for GRB 221009A followed the same process as described in Zhang et al. (2011) and Yang et al. (2022). First, we retrieved the time-tagged event data set covering the time range of GRB 221009A from the Fermi/GBM public data archive.[15] Next, we selected three sodium iodide (NaI) detectors (namely n6, n7, and n8) and one bismuth germanium oxide (BGO) detector (b1) with optimal viewing angles for spectral analysis and divided the precursor episode into 12 time slices with equal signal-to-noise levels. For each combination of detector and time slice, the source spectrum and background spectrum were obtained by summing up the number of total photons and background photons for each energy channel, respectively. The number of background photons was determined by simulating the background level using the baseline algorithm[16] on each energy channel. Furthermore, the detector response matrix in the direction of GRB 221009A was generated using the *gbm_drm_gen*[17] package (Burgess et al. 2018; Berlato et al. 2019).

An et al. (2023) provides a comprehensive description of the data reduction and analysis procedure for SATech-01/GECAM-C. Here, we highlight some key notes. Each GRD detector contains two independent modes, namely high-gain (6–300 keV) and low-gain (0.4–6 MeV), which cover a considerable energy range spanning 3 orders of magnitude. During the main emission episode, we partitioned the time range from $T_0 + 220$ to $T_0 + 272$ s into 40 time slices. For the flare episode, we selected 11 time slices within a 20 s time window around the peak, which contains most of the significant radiation. We then acquired source spectra, background spectra, and response matrices for both high- and low-gain channels for each time slice for spectral analysis. It is worth noting that there is an issue with inaccurate dead time recording in the high-gain data, but this does not distort the spectral shape. Therefore, we utilized the low-gain spectrum as a reference and applied a scaling factor to the high-gain spectrum in each time slice.

3. The Synchrotron Model

Consider an ultrarelativistic thin shell ejected from the GRB central engine, within which the magnetic field is entrained with the ejected material and electrons are accelerated into a power-law distribution with an index of p, given by $\frac{dN_e}{d\gamma_e} \propto \gamma_e^{-p}$, through mechanisms such as magnetic dissipation (Zhang & Yan 2011). Upon injection, the electrons will primarily undergo cooling through synchrotron and adiabatic processes toward lower energies, while inverse Compton cooling is typically negligible due to the Klein–Nishina effect and, therefore, not taken into account. The continuity equation of electrons is

$$\frac{\partial}{\partial t'}\left(\frac{dN_e}{d\gamma_e}\right) + \frac{\partial}{\partial \gamma_e}\left[\dot{\gamma}_e\left(\frac{dN_e}{d\gamma_e}\right)\right] = Q(\gamma_e, t'), \quad (1)$$

where $Q(\gamma_e, t')$ is the injection rate of electrons, which is the function of electron energy γ_e and time t' in the comoving frame of the shell, and reads as

$$Q(\gamma_e, t') = \begin{cases} Q_0\left(\frac{t'}{t'_0}\right)^q \gamma_e^{-p}, & \gamma_{\min} < \gamma_e < \gamma_{\max}, \\ 0, & \text{otherwise} \end{cases} \quad (2)$$

[15] https://heasarc.gsfc.nasa.gov/FTP/fermi/data/gbm/daily/
[16] https://github.com/derb12/pybaselines
[17] https://github.com/grburgess/gbm_drm_gen

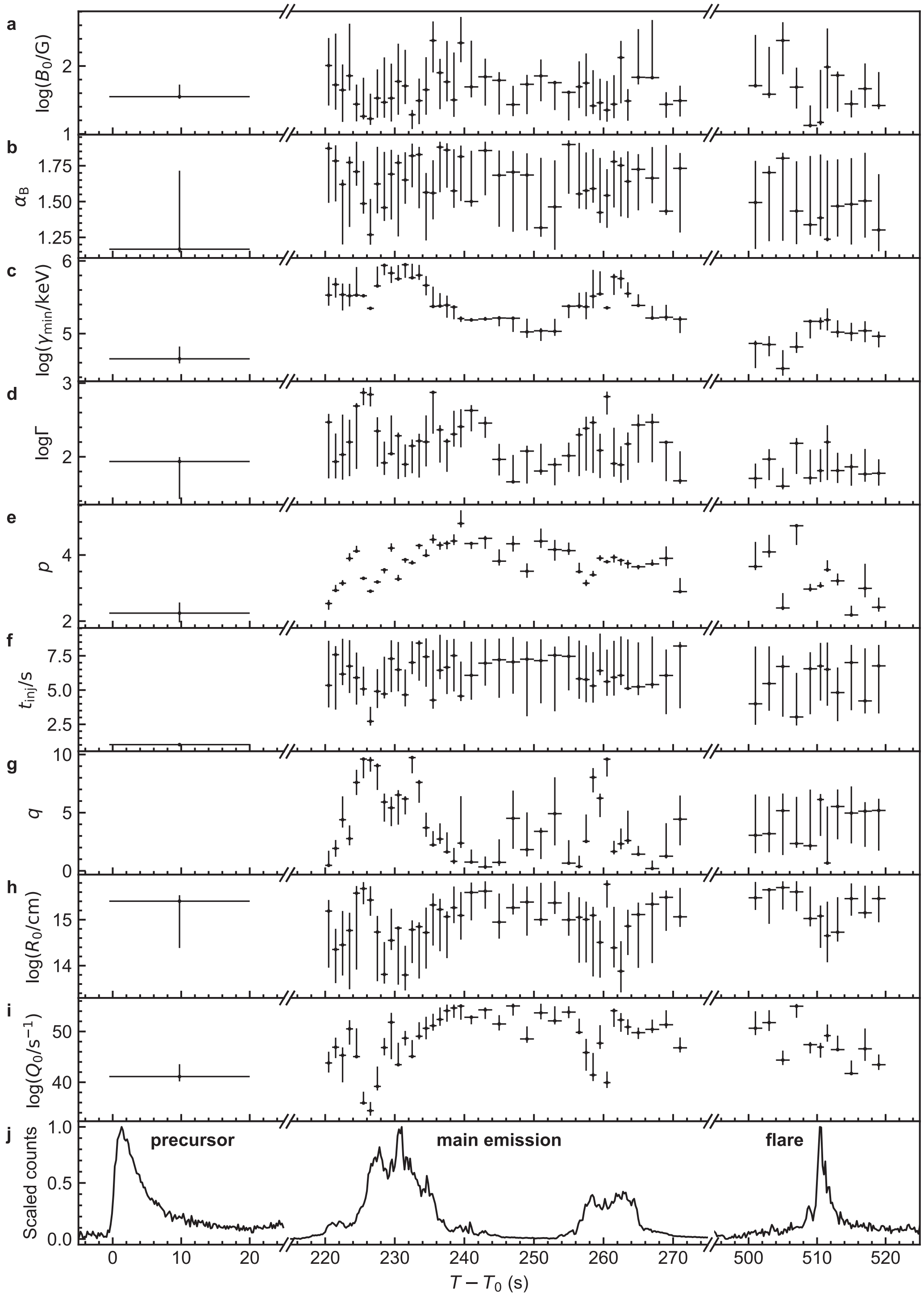

Figure 1. The observed light curve of GRB 221009A and its spectral evolution as reflected by the best-fit parameters of our synchrotron model. (a)–(i) The best-fit values and 1σ uncertainties of the nine model parameters for all time slices in the precursor, main emission, and flare episodes. (j) The scaled light curves derived from Fermi/GBM data for precursor, and SATech-01/GECAM-C data for main emission and flare.

where Q_0 is the injection coefficient, and $\gamma_{\rm min}$ and $\gamma_{\rm max}$ are the minimum and maximum Lorentz factor of the injected electrons, respectively. Here we consider the injection rate increases with a power law in time (Zhang et al. 2016) and ceases at an observed time $t_{\rm inj} = (1 + z)(R_{\rm inj} - R_0)/2\Gamma^2 c$, where R_0 and $R_{\rm inj}$ are respectively the initial radius where GRB emission begins to be generated and the radius where the injection ceases. Note that we adopt the convention that the comoving frame, the electron energy, magnetic field (B), injection rate, and electron distribution are unprimed although they are measured in the shell comoving frame. The synchrotron cooling and adiabatic cooling rate are given by

$$\dot{\gamma}_{\rm e,tot} = \dot{\gamma}_{\rm e,syn} + \dot{\gamma}_{\rm e,adi} = -\frac{\sigma_{\rm T} B^2 \gamma_{\rm e}^2}{6\pi m_{\rm e} c} - \frac{2\gamma_{\rm e}}{3(t' + t_0')}, \quad (3)$$

where $t_0' = \frac{t_0}{\Gamma} = \frac{R_0}{\Gamma \beta_\Gamma c}$ is the initial time in the comoving frame of the shell, t_0 is the initial time in the burst source frame where GRB emission begins to be generated. In addition, $\Gamma = \frac{1}{\sqrt{1-\beta_\Gamma^2}}$ is the bulk Lorentz factor, c is the light speed, m_e is the electron mass, and σ_T is Thomson scattering cross section. Due to the conservation of magnetic flux, the magnetic field within the shell will decrease as the emission region expands (Spruit et al. 2001). The exact decay form of the magnetic field depends on the unknown magnetic field configuration. For simplicity, we adopt the following generalized form to describe the magnetic field decay behaviors:

$$B = B_0 \left(\frac{t'}{t_0'}\right)^{-\alpha_B}, \tag{4}$$

where B_0 is the initial magnetic field and α_B is the decaying index.

The synchrotron radiation power in the comoving frame is (Rybicki & Lightman 1979)

$$P'(\nu') = \frac{\sqrt{3}\, q_e^3 B}{m_e c^2} \int_{\gamma_{\min}}^{\gamma_{\max}} \left(\frac{dN_e}{d\gamma_e}\right) F\left(\frac{\nu'}{\nu_c'}\right) d\gamma_e, \tag{5}$$

where $\nu_c' = 3 q_e B \gamma_e^2 / (4\pi m_e c)$, $F(x) = x \int_x^{+\infty} K_{5/3}(k) dk$, $K_{5/3}(k)$ is the Bessel function, and q_e is the electron charge. Considering the equal-arrival-time surface effect (e.g., Sari 1998), the observed specific flux can be obtained by

$$F_{\nu_{\rm obs}} = \frac{1+z}{4\pi D_L^2} \int_{t_0}^{t_e} \frac{c}{2R} \frac{P'(\nu'(\nu_{\rm obs}))}{\Gamma^3 (1 - \beta_\Gamma \cos\theta)^2} dt, \tag{6}$$

where $\nu_{\rm obs} = \nu' \mathcal{D}/(1+z)$ is observed photon frequency, $\mathcal{D} = 1/[\Gamma(1 - \beta_\Gamma \cos\theta)]$ is Doppler factor, θ is the angle between the velocity of an infinitesimal volume of the jet and line of sight, $t_e = t_0 + t/(1+z)/(1-\beta_\Gamma)$ is the time in the burst source frame corresponding to observed time t and D_L is the luminosity distance obtained by adopting a flat ΛCDM universe with $H_0 = 67.4\ {\rm km\ s^{-1}\ Mpc^{-1}}$, $\Omega_m = 0.315$, and $\Omega_\Lambda = 0.685$ (Planck Collaboration et al. 2020).

Substituting Equations (1)–(5) to (6), we can obtain the final observed flux predicted by our model in the form of

$$F_{\nu_{\rm obs}} = F_{\nu_{\rm obs}}(t, \nu, B_0, \alpha_B, \gamma_{\min}, \Gamma, p, t_{\rm inj}, q, R_0, Q_0, \gamma_{\max}, z). \tag{7}$$

In this study, we keep $\gamma_{\max}$ fixed at 10^8. So, the final free parameter set, $\mathcal{P}$, of Equation (7) includes the following nine terms:

1. The initial radius R_0 in units of centimeters where the GRB emission begins to be generated.
2. The initial magnetic field strength B_0 in units of gauss at the initial radius of the emission region.
3. The power-law decay index α_B of the magnetic field.
4. The bulk Lorentz factor Γ of the emission region.
5. The minimum Lorentz factor $\gamma_{\min}$ of injected electrons.
6. The power-law index p of the injected electron spectrum.
7. The power-law index q of the injection rate of electrons as a function of t'.
8. The injection time $t_{\rm inj}$ in observer's frame in units of seconds.
9. The electron injection rate coefficient Q_0 in units of s^{-1}.

Table 1
The Prior Bound of Each Model Parameter for Spectral Fitting

Parameters	Prior Bounds	
	Precursor	Main Emission and Flare
$\log(B_0/{\rm G})$	[0, 3]	[1, 3]
α_B	[1, 2]	[1, 2]
$\log\gamma_{\min}$	[4, 7]	[3, 6]
$\log\Gamma$	[1.2, 3.0]	[1.5, 3.0]
p	[1.5, 3.5]	[2, 6]
$t_{\rm inj}/{\rm s}$	[−0.5, 2.0]	[0, 10]
q	(0)	[0, 10]
$\log(R_0/{\rm cm})$	[12, 16]	[12, 16]
$\log(Q_0/{\rm s^{-1}})$	[31, 56]	[28, 56]

Adapting the prior bounds as listed in Table 1, We can then fit our synchrotron model, namely,

$$F_{\nu_{\rm obs}} = F_{\nu_{\rm obs}}(t, \nu, \mathcal{P}), \tag{8}$$

to the observed spectra at t in the observer frame.

4. The Fit

In accordance with the methodology outlined in Yang et al. (2022), we utilize our self-developed Python package, MySpecFit, to fit all the spectral data with our model as described in Equation (8). MySpecFit implements Bayesian parameter estimation by wrapping PyMultinest (Buchner et al. 2014), a Python interface to the popular Fortran nested sampling implementation Multinest (Feroz & Hobson 2008; Feroz et al. 2009; Buchner et al. 2014; Feroz et al. 2019). Multinest begins by drawing a set of points in parameter space, called live points, and creating ellipsoids around them. The likelihood is evaluated at each live point, and the point with the lowest likelihood is removed, while new point with higher likelihood is generated in the ellipsoids around the remaining live points, until the exploration ends in a sufficiently small sampling volume. Multinest excels in sampling and evidence evaluation from distributions that may contain multiple modes and highly degeneracy, and performs well in low to moderate dimensional parameter spaces. In MySpecFit, PGSTAT[18] (Arnaud 1996) is employed as a statistical metric to evaluate the likelihood, which is appropriate for Poisson data in the source spectrum with Gaussian background in the background spectrum.

4.1. Time-dependent Fit to the Precursor

To apply Equation (8) in its simplest form, one can assume that only one single electron ejection event occurs and solve Equation (8) for each time step to obtain a series of spectra for any given observation time, $t_{\rm obs}$. This approach is only suitable for observation data that has a temporal shape resembling a single pulse, which is the case for the precursor of GRB 221009A. We are thus motivated to fit the observed time-resolved spectra of the complete time series of precursor episode with the time-involved model $F(t, \nu, \mathcal{P})$, where $\mathcal{P}$ represents the single set of parameters described above.

Interestingly, our initial attempts using broad prior ranges (see Table 1) show that the posterior distribution of q was

[18] https://heasarc.gsfc.nasa.gov/xanadu/xspec/

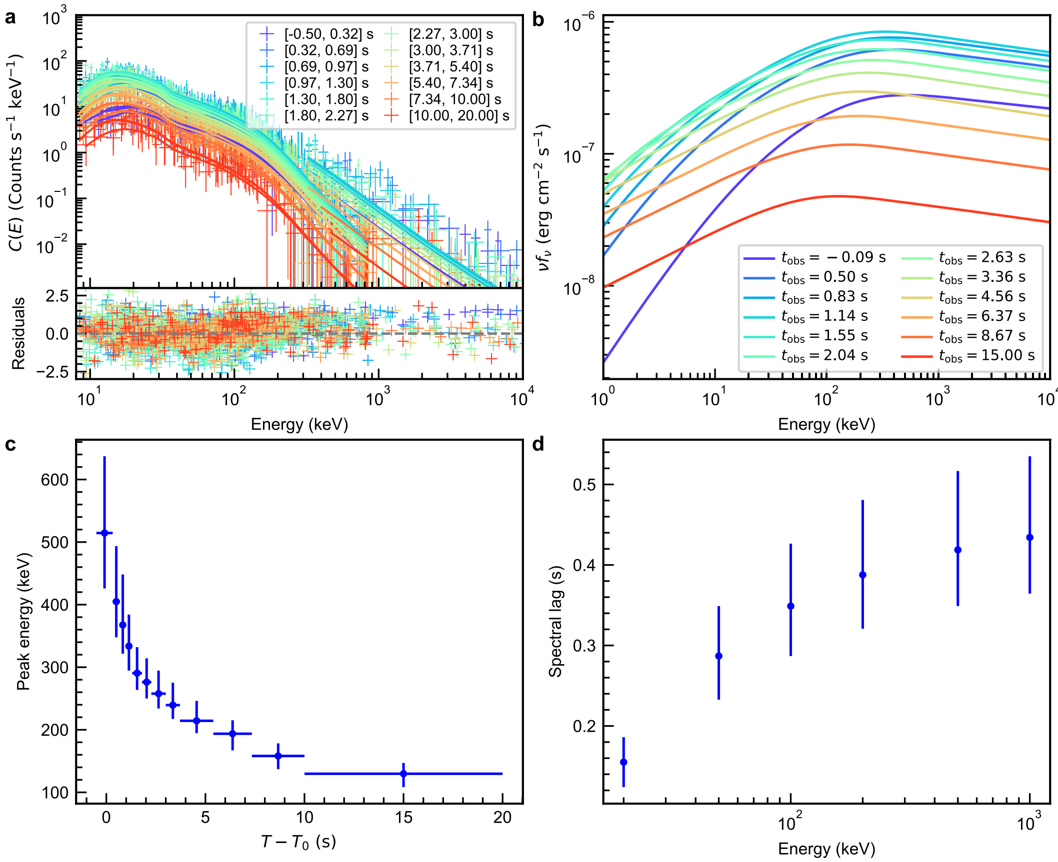

Figure 2. The synchrotron fit for the precursor episode. (a) The observed and modeled photon count spectra. (b) The evolution of the νf_ν spectra as a function of the observed times. (c) The evolution of peak energies derived from the νf_ν spectra. (d) The evolution of spectral lags as a function of the energies. All error bars represent the 1σ confidence level.

centered around zero, indicating that electrons are injected into the emission region at a constant rate during the precursor episode. Thus, we fix q at zero for the time-resolved fit. After achieving a successful fit with statistically acceptable goodness of fit values (i.e., PGSTAT/degrees of freedom (dof) $\sim$1), we listed the best-fit parameters, their 1σ uncertainties (see also Figure 1), and fit goodness in Table B1. Figure 2(a) exhibits the comparison between the data and the model. The observed time-dependent νf_ν spectra predicted by the best-fit synchrotron model are displayed in Figures 2(b). Furthermore, we reproduce the observed hard-to-soft spectral evolution and hundreds of milliseconds of spectral lags, as shown in Figures 2(c) and (d), respectively. Figure A1 displays the corresponding corner plot of the posterior probability distributions of the parameters for the fit of the synchrotron model to the precursor. We note that most of the parameters are well constrained, except that Γ and R_0 exhibit a bimodal distribution. The best-fit values for both Γ and R_0 fall on the component with a higher probability.

4.2. Time-independent Fit to Main Emission and Flare

As depicted in Figure 1, the main emission and flare episodes exhibit intricate and variable temporal profiles that consist of multiple simple pulses superimposed on each other, which implies multiple continuous activities of the central engine. Therefore, it is unrealistic to describe their complete evolutionary features using one set of parameters with a single electron ejection event. Hence, we assume that each time slice corresponds to a completely independent ejection and radiation process and fit them independently using Equation (8), a method also employed in Zhang et al. (2016). This approach enables us to explore the temporal evolution of the model parameters in a slice-wise manner.

By leaving q free and utilizing the prior bounds listed in Table 1, we obtained the best-fit parameter sets, their uncertainties (see also Figure 1), and corresponding statistics, as listed in Table B1. The PGSTAT/dof values are generally around 1, indicating good fits. Figure 1 illustrates the evolution of each best-fit parameter. As examples, in Figures 3(a) and (c), we present the observed versus modeled photon count spectra for the brightest time slices during the main emission and flare episodes, respectively. The evolution of the νf_ν spectra during the main emission and the flaring episodes as a function of the observed times are shown in Figures 3(b) and (d), respectively.

5. Conclusions and Implications

We successfully fit the observed time-resolved spectra of GRB 221009A using a physical model that incorporates synchrotron radiation of a bulk of relativistic electrons that are accelerated in a large emission region under a decaying magnetic field. Our model successfully reproduced the nonthermal spectra as observed (Figures 2 and 3). The $E_{\rm p}$ values, or the $\nu F\nu$ peak, measured by our physical model, fall within the range of 255 keV to 3.4 MeV, which is in line with the values presented in An et al. (2023) and Frederiks et al. (2023). Using the best-fit parameters, our model can also

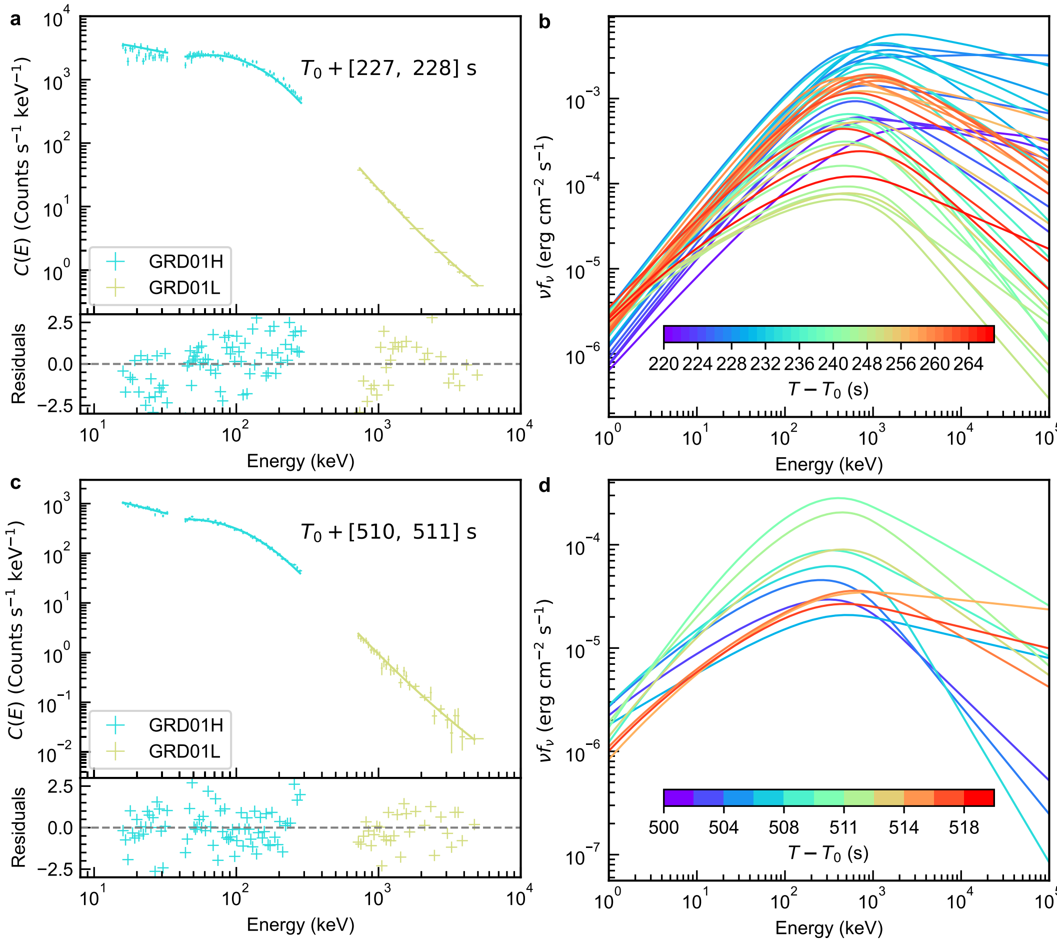

Figure 3. The synchrotron fit for the main emission and flare episodes. (a) The observed and modeled photon count spectra during the brightest time slice of the main emission episode. (b) The evolution of the νf_ν spectra during main emission as a function of the observed times. (c) The observed and modeled photon count spectra during the brightest time slice of flare episode. (d) The evolution of the νf_ν spectra during the flare as a function of the observed times.

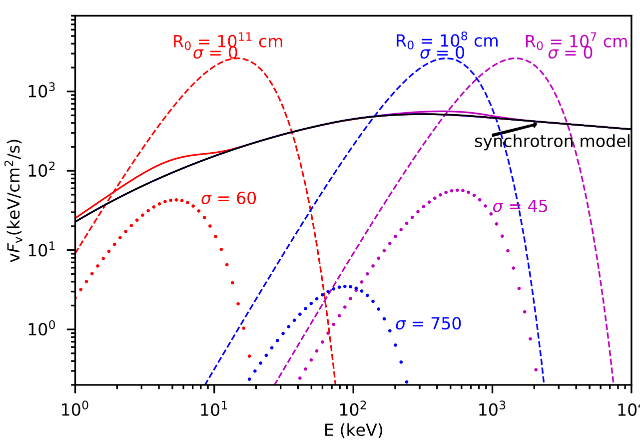

Figure 4. Calculation of σ. The synchrotron spectrum for the time slice between 0.975 and 1.305 s is shown as a black solid line. The colored dashed and dotted lines represent synthetic blackbody components with σ values being zero or a lower limit value above which the photosphere emission is not observable, respectively. The colored solid lines represent the hybrid model composed of the synchrotron (black line) and blackbody components (colored dotted line) with the lower limit value of σ. The unknown size of the jet base at the central engine is adopted as three different values, i.e., $R_0 = 10^7,\ 10^8,\ 10^{11}$ cm, which are denoted with the purple, blue and red, respectively. The derived lower limit values of σ are 45, 750, and 60, respectively.

reproduce the observed hard-to-soft spectral evolution and spectral lags during the precursor (see Figure 2).

Our findings indicate that the emission region is approximately 10^{15} cm in size, and the magnetic field ranges from a few tens to a few hundred gauss. This configuration aligns with the scenario that the ejecta is a Poynting flux-dominated outflow (Zhang & Yan 2011). Within this scenario, the timescale corresponding to the curvature effect is defined by the duration of the broad pulses. The rapid variability in the light curves is related to the minijets due to turbulent reconnection in the emission region (e.g., Zhang & Zhang 2014; Shao & Gao 2022). Applying the Bayesian method (Scargle et al. 2013), we derive the shortest variability timescale of about 0.12 s, which is much shorter than the timescale defined by the emission radius. This is fully consistent with the ICMART picture of Zhang & Yan (2011).

The Poynting flux–dominated nature of the outflow can also be demonstrated by calculating the ratio of the Poynting flux's luminosity to the baryonic flux's luminosity, denoted by σ (Zhang & Pe'er 2009). Specifically, σ is defined as $\sigma \equiv L_P/L_b$. A high value of σ indicates that the Poynting flux is the primary energy source. If the flow is baryonic flux dominated, one would observe a blackbody spectrum with a temperature

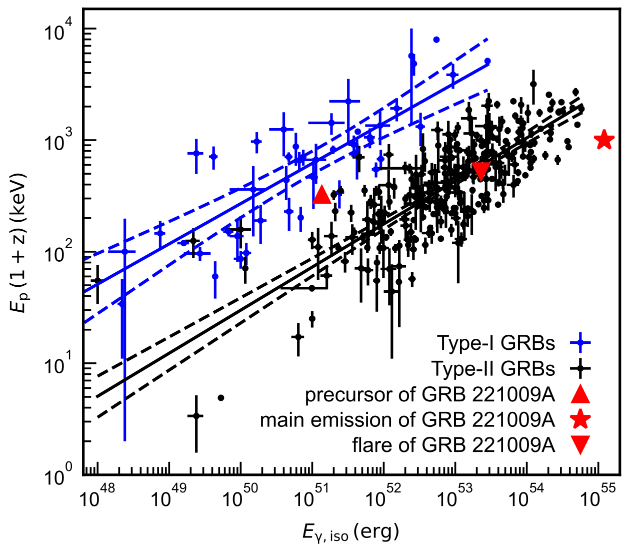

Figure 5. The $E_p(1+z)$ and $E_{\gamma,\text{iso}}$ correlation diagram. The best-fit correlations (solid lines) and corresponding 3σ confidence bands (dashed lines) are presented for Type I (compact star merger origin) and Type II (massive star core-collapse origin) GRB populations with blue and black colors, respectively (see Zhang et al. 2009 for a detailed discussion of the Type I/II classification scheme). The precursor, main emission, and flare episodes of GRB 221009A are denoted by a filled triangle, star, and filled upside-down triangle, respectively. Error bars on data points represent the 1σ confidence level.

estimated as $T_{\rm ph}^{\rm ob} = (L_{\rm w}/4\pi R_0^2 ca)^{1/4}(1+z)^{-1}$, where $L_{\rm w}$ is the initial wind luminosity of the fireball, R_0 is the radius of the fireball base, c is the speed of light, and a is the Stefan–Boltzmann energy density constant. We tested this hypothesis by setting the initial wind luminosity $L_{\rm w}$ to be equal to the gamma-ray luminosity L_γ in the time slice between $T_0 + 0.975$ s and $T_0 + 1.305$ s of the precursor, and calculating the blackbody spectrum at $R_0 = 10^7$, 10^8, 10^{11} cm, respectively, which are represented by dashed lines in Figure 4. Obviously, all of these spectra had significant thermal-like peaks that were not present in the observed data.

Next, we investigated the maximal level at which the baryonic flux is allowed so the blackbody component, if any, is barely suppressed. This approach allows placing a lower limit onto σ (Zhang & Pe'er 2009). To do so, we first generate the blackbody spectrum given the different σ by replacing $L_{\rm w}$ with $L_\gamma/(1+\sigma)$, as plotted as dotted lines in Figure 4. We added this blackbody spectrum to our best-fit physical spectrum and determined its goodness of fit to the observed data. By using the Akaike Information Criterion (AIC; Akaike 1974; Sugiura 1978), we could determine the σ value at which the hybrid model deviated significantly from the observation (ΔAIC > 5; Krishak & Desai 2020). Our calculations with different R_0 values all yielded a global lower limit of $\sigma \geqslant 45$, which strongly suggests that the outflow is dominated by Poynting flux.

By using the average $E_{\rm p}$ and flux values for each episode, we can determine the burst energies and plot them on the $E_{\rm p,z}$–$E_{\gamma,\rm iso}$ diagram (Amati et al. 2002; Zhang et al. 2009; Minaev & Pozanenko 2020), which is depicted in Figure 5. Notably, even with the energy of only the main emission considered, GRB 221009A ranks as the most energetic burst with $E_{\gamma,\rm iso} \sim 1.21 \times 10^{55}$ erg within the energy range between 1 keV and 10 MeV (see also An et al. 2023), despite being an extraordinary GRB that follows the same track as other Type II GRBs in the diagram.

We acknowledge the support by the National Key Research and Development Programs of China (2018YFA0404204, 2021YFA0718500, 2022YFF0711404, 2022SKA0130102), the National Natural Science Foundation of China (grant Nos. 11833003, U2038105, U1831135, 12121003, 12273042), the National SKA Program of China (2022SKA0130100), the science research grants from the China Manned Space Project with NO.CMS-CSST-2021-B11, the Fundamental Research Funds for the Central Universities, the Program for Innovative Talents, and the Strategic Priority Research Program on Space Science, the Chinese Academy of Sciences, grant No. XDB23040400.

Appendix A
The Posterior Probability Distributions for the Fit to the Precursor

Figure A1 displays the corner plot of the posterior probability distributions of the parameters for the fit of the synchrotron model to the precursor episode.

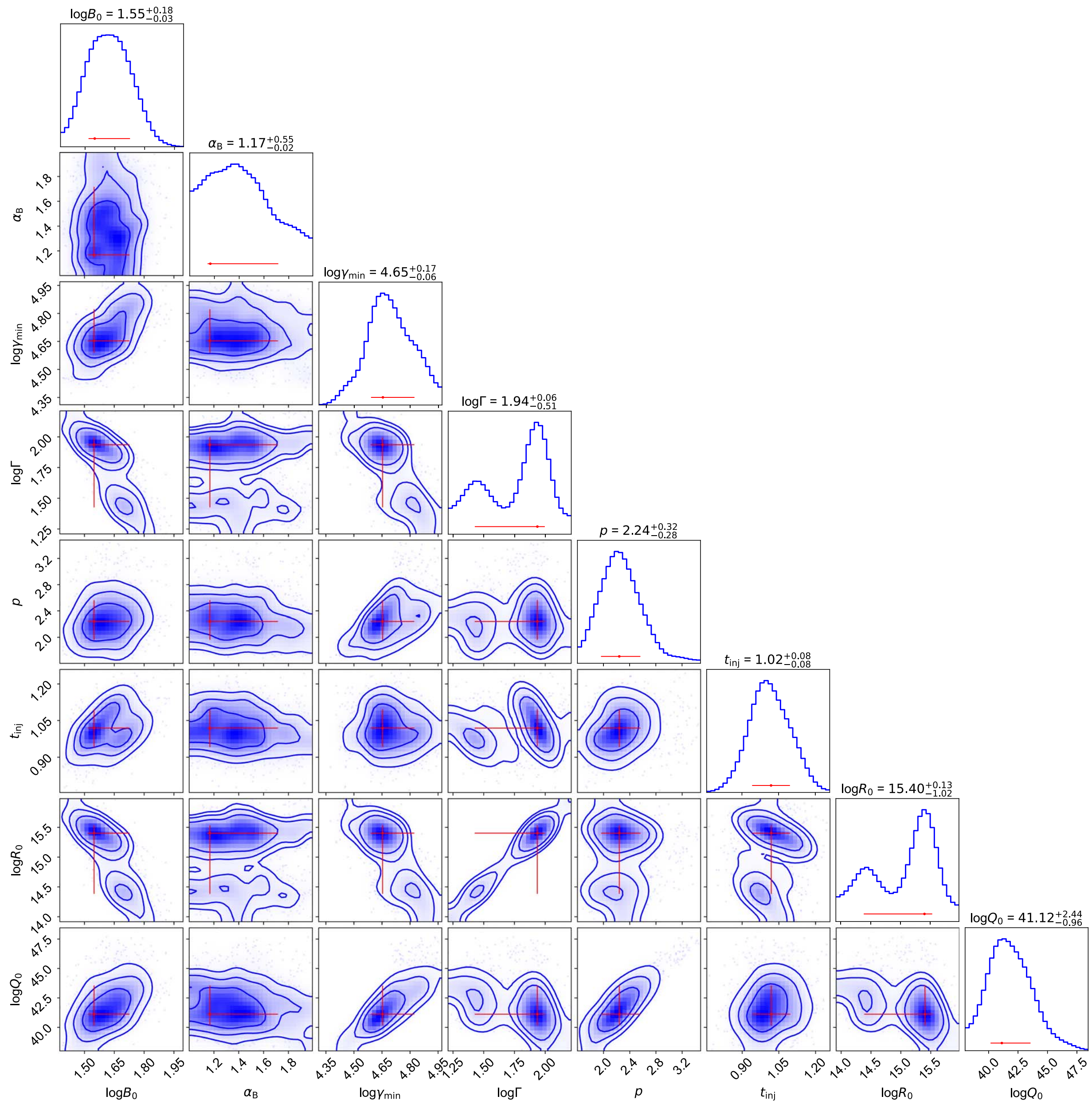

Figure A1. Corner plot of the posterior probability distributions of the parameters for the fit of the synchrotron model to the precursor. The red error bars represent 1σ uncertainties.

Appendix B
Spectral Fitting Results

The best-fit parameters, their 1σ uncertainties, and corresponding fit goodness are listed in Table B1. We also list the peak energies in the νf_ν spectra derived from our physical models.

Table B1
Spectral Fitting Results and Derived Peak Energies in Each Time Slice

$t1$ (s)	$t2$ (s)	log (B_0) (G)	α_B	logγ_{min}	logΓ	p	t_{inj} (s)	q	log (R_0) (cm)	log (Q_0) (s^{-1})	PGSTAT/dof	E_p (keV)
−0.50	20.00	$1.55^{+0.18}_{-0.03}$	$1.17^{+0.55}_{-0.02}$	$4.65^{+0.17}_{-0.06}$	$1.94^{+0.06}_{-0.51}$	$2.24^{+0.32}_{-0.28}$	$1.02^{+0.08}_{-0.08}$	(0)	$15.40^{+0.13}_{-1.02}$	$41.12^{+2.44}_{-0.96}$	4087.90/5824.00	281.70 ± 13.79
220.00	221.00	$2.01^{+0.41}_{-0.59}$	$1.87^{+0.04}_{-0.38}$	$5.53^{+0.25}_{-0.15}$	$2.47^{+0.11}_{-0.76}$	$2.53^{+0.11}_{-0.19}$	$5.34^{+3.26}_{-1.61}$	$0.47^{+1.26}_{-0.03}$	$15.19^{+0.24}_{-1.23}$	$43.80^{+2.21}_{-1.89}$	273.95/128.00	$3409.62^{+4168.73}_{-547.48}$
221.00	222.00	$1.72^{+0.76}_{-0.37}$	$1.78^{+0.11}_{-0.28}$	$5.68^{+0.09}_{-0.18}$	$1.93^{+0.38}_{-0.23}$	$2.93^{+0.17}_{-0.05}$	$7.58^{+0.63}_{-4.01}$	$1.93^{+0.73}_{-0.72}$	$14.35^{+0.45}_{-0.73}$	$46.90^{+1.89}_{-2.14}$	201.86/128.00	$1179.27^{+110.63}_{-37.42}$
222.00	223.00	$1.65^{+0.38}_{-0.47}$	$1.62^{+0.03}_{-0.42}$	$5.54^{+0.15}_{-0.22}$	$2.03^{+0.54}_{-0.34}$	$3.15^{+0.10}_{-0.08}$	$6.16^{+2.58}_{-0.80}$	$4.39^{+2.01}_{-0.67}$	$14.45^{+0.74}_{-0.67}$	$45.31^{+1.56}_{-5.33}$	275.35/128.00	$773.71^{+72.71}_{-5.33}$
223.00	224.00	$1.86^{+0.77}_{-0.22}$	$1.77^{+0.04}_{-0.45}$	$5.52^{+0.16}_{-0.15}$	$2.20^{+0.30}_{-0.46}$	$3.90^{+0.16}_{-0.09}$	$6.74^{+1.90}_{-1.96}$	$2.77^{+1.14}_{-0.58}$	$14.77^{+0.39}_{-1.28}$	$50.51^{+1.72}_{-3.10}$	203.28/128.00	$666.14^{+23.41}_{-17.05}$
224.00	225.00	$1.44^{+0.29}_{-0.25}$	$1.71^{+0.21}_{-0.10}$	$5.53^{+0.39}_{-0.01}$	$2.69^{+0.04}_{-0.85}$	$4.12^{+0.16}_{-0.04}$	$5.90^{+1.83}_{-1.96}$	$7.60^{+1.09}_{-1.08}$	$15.58^{+0.16}_{-1.66}$	$45.05^{+5.57}_{-0.25}$	249.74/128.00	$627.42^{+17.58}_{-5.75}$
225.00	226.00	$1.26^{+0.57}_{-0.05}$	$1.49^{+0.30}_{-0.07}$	$5.52^{+0.01}_{-0.01}$	$2.87^{+0.06}_{-0.17}$	$3.29^{+0.03}_{-0.04}$	$5.08^{+1.63}_{-0.49}$	$9.61^{+0.01}_{-1.65}$	$15.68^{+0.14}_{-0.34}$	$35.92^{+2.22}_{-0.24}$	397.10/128.00	$902.80^{+23.16}_{-8.28}$
226.00	227.00	$1.22^{+0.37}_{-0.09}$	$1.27^{+0.25}_{-0.07}$	$5.35^{+0.01}_{-0.01}$	$2.85^{+0.10}_{-0.16}$	$2.90^{+0.01}_{-0.04}$	$2.72^{+1.06}_{-0.31}$	$9.52^{+0.27}_{-0.99}$	$15.43^{+0.30}_{-0.34}$	$34.40^{+1.71}_{-0.99}$	397.10/128.00	unconstrained
227.00	228.00	$1.53^{+0.42}_{-0.29}$	$1.62^{+0.26}_{-0.21}$	$5.66^{+0.27}_{-0.00}$	$2.35^{+0.19}_{-0.48}$	$3.18^{+0.05}_{-0.04}$	$4.91^{+1.62}_{-1.22}$	$9.04^{+0.19}_{-2.09}$	$14.73^{+0.35}_{-1.07}$	$39.18^{+3.92}_{-0.80}$	307.21/128.00	[1053.43, 1126.19]
228.00	229.00	$1.47^{+0.66}_{-0.23}$	$1.46^{+0.39}_{-0.09}$	$5.94^{+0.02}_{-0.13}$	$1.92^{+0.29}_{-0.16}$	$3.55^{+0.01}_{-0.11}$	$4.72^{+2.72}_{-0.33}$	$5.91^{+0.73}_{-1.68}$	$13.81^{+0.70}_{-0.20}$	$46.83^{+1.90}_{-1.53}$	258.35/128.00	[1505.34, 1579.94]
229.00	230.00	$1.53^{+0.51}_{-0.34}$	$1.69^{+0.17}_{-0.32}$	$5.83^{+0.09}_{-0.14}$	$2.04^{+0.52}_{-0.02}$	$4.21^{+0.15}_{-0.11}$	$7.29^{+1.35}_{-2.44}$	$5.42^{+0.94}_{-1.58}$	$14.55^{+0.69}_{-0.21}$	$51.81^{+1.86}_{-7.27}$	205.38/128.00	$1491.54^{+38.27}_{-23.85}$
230.00	231.00	$1.77^{+0.56}_{-0.49}$	$1.77^{+0.06}_{-0.51}$	$5.75^{+0.19}_{-0.03}$	$2.29^{+0.04}_{-0.59}$	$3.27^{+0.13}_{-0.06}$	$6.48^{+2.02}_{-1.58}$	$6.52^{+0.42}_{-2.55}$	$14.82^{+0.03}_{-1.23}$	$43.46^{+4.32}_{-0.27}$	186.54/128.00	[2156.09, 2289.14]
231.00	232.00	$1.71^{+0.53}_{-0.27}$	$1.65^{+0.19}_{-0.17}$	$5.95^{+0.00}_{-0.18}$	$1.90^{+0.27}_{-0.17}$	$3.86^{+0.03}_{-0.09}$	$4.65^{+1.85}_{-0.85}$	$6.19^{+0.23}_{-1.34}$	$13.80^{+0.64}_{-0.34}$	$48.68^{+1.44}_{-1.44}$	253.97/128.00	$1338.52^{+37.51}_{-6.15}$
232.00	233.00	$1.28^{+0.07}_{-0.21}$	$1.82^{+0.09}_{-0.22}$	$5.77^{+0.19}_{-0.01}$	$2.15^{+0.09}_{-0.37}$	$3.76^{+0.07}_{-0.01}$	$7.01^{+1.55}_{-0.85}$	$9.73^{+0.06}_{-1.35}$	$14.78^{+0.20}_{-0.73}$	$45.09^{+3.22}_{-0.38}$	324.62/128.00	$780.87^{+18.19}_{-1.80}$
233.00	234.00	$1.49^{+0.33}_{-0.35}$	$1.83^{+0.05}_{-0.38}$	$5.80^{+0.14}_{-0.07}$	$2.21^{+0.10}_{-0.50}$	$4.29^{+0.04}_{-0.11}$	$8.43^{+0.19}_{-2.75}$	$7.61^{+0.20}_{-1.76}$	$14.85^{+0.10}_{-1.13}$	$49.05^{+2.77}_{-0.63}$	240.13/128.00	$854.25^{+11.89}_{-9.78}$
234.00	235.00	$1.65^{+0.48}_{-0.37}$	$1.56^{+0.14}_{-0.34}$	$5.66^{+0.13}_{-0.14}$	$2.20^{+0.36}_{-0.33}$	$3.99^{+0.18}_{-0.04}$	$7.43^{+1.34}_{-2.19}$	$3.71^{+1.30}_{-0.78}$	$14.72^{+0.54}_{-0.78}$	$50.62^{+2.28}_{-2.16}$	287.75/128.00	$1001.38^{+23.33}_{-11.47}$
235.00	236.00	$2.38^{+0.28}_{-0.47}$	$1.56^{+0.23}_{-0.18}$	$5.37^{+0.27}_{-0.00}$	$2.87^{+0.00}_{-0.56}$	$4.47^{+0.16}_{-0.12}$	$4.27^{+3.65}_{-0.63}$	$2.23^{+1.19}_{-0.02}$	$15.32^{+0.25}_{-0.88}$	$51.14^{+2.36}_{-0.98}$	381.81/128.00	$978.58^{+29.74}_{-6.74}$
236.00	237.00	$1.90^{+0.20}_{-0.54}$	$1.88^{+0.04}_{-0.31}$	$5.38^{+0.18}_{-0.01}$	$2.37^{+0.06}_{-0.44}$	$4.30^{+0.10}_{-0.14}$	$6.45^{+2.59}_{-0.65}$	$2.73^{+1.35}_{-0.42}$	$15.22^{+0.23}_{-0.91}$	$52.37^{+2.37}_{-1.25}$	260.79/128.00	$606.12^{+21.30}_{-2.79}$
237.00	238.00	$1.77^{+0.60}_{-0.29}$	$1.86^{+0.05}_{-0.26}$	$5.39^{+0.13}_{-0.17}$	$2.21^{+0.03}_{-0.41}$	$4.35^{+0.08}_{-0.18}$	$6.66^{+2.00}_{-1.95}$	$1.63^{+1.68}_{-0.10}$	$15.07^{+0.12}_{-0.90}$	$54.09^{+1.21}_{-2.17}$	225.66/128.00	$527.89^{+20.08}_{-7.24}$
238.00	239.00	$1.50^{+0.70}_{-0.25}$	$1.57^{+0.29}_{-0.12}$	$5.37^{+0.02}_{-0.17}$	$2.31^{+0.32}_{-0.17}$	$4.42^{+0.20}_{-0.12}$	$7.51^{+1.22}_{-2.62}$	$0.82^{+1.16}_{-0.23}$	$15.26^{+0.46}_{-0.34}$	$54.63^{+0.67}_{-1.94}$	211.74/128.00	$513.50^{+11.96}_{-16.29}$
239.00	240.00	$2.34^{+0.38}_{-0.28}$	$1.81^{+0.08}_{-0.31}$	$5.21^{+0.03}_{-0.05}$	$2.41^{+0.24}_{-0.28}$	$4.95^{+0.40}_{-0.12}$	$4.56^{+2.52}_{-0.36}$	$2.38^{+4.04}_{-0.41}$	$15.09^{+0.51}_{-0.53}$	$55.00^{+0.34}_{-2.69}$	172.58/128.00	$569.58^{+18.66}_{-11.68}$
240.00	242.00	$1.69^{+0.68}_{-0.15}$	$1.50^{+0.35}_{-0.04}$	$5.19^{+0.03}_{-0.00}$	$2.63^{+0.07}_{-0.28}$	$4.35^{+0.06}_{-0.16}$	$6.07^{+2.46}_{-1.78}$	$0.75^{+1.08}_{-0.10}$	$15.59^{+0.22}_{-0.61}$	$52.80^{+0.37}_{-1.39}$	204.72/128.00	$436.04^{+4.04}_{-14.81}$
242.00	244.00	$1.84^{+0.27}_{-0.42}$	$1.86^{+0.06}_{-0.31}$	$5.20^{+0.03}_{-0.01}$	$2.46^{+0.09}_{-0.20}$	$4.50^{+0.08}_{-0.32}$	$6.96^{+1.77}_{-1.64}$	$0.34^{+0.89}_{-0.18}$	$15.62^{+0.22}_{-0.38}$	$54.26^{+0.48}_{-1.81}$	144.11/128.00	$436.04^{+4.04}_{-14.81}$
244.00	246.00	$1.79^{+0.12}_{-0.50}$	$1.68^{+0.17}_{-0.36}$	$5.21^{+0.03}_{-0.11}$	$1.96^{+0.21}_{-0.22}$	$3.81^{+0.36}_{-0.13}$	$7.21^{+1.55}_{-2.78}$	$0.73^{+1.98}_{-0.31}$	$14.95^{+0.62}_{-0.36}$	$51.48^{+1.74}_{-1.29}$	168.11/128.00	$453.45^{+25.77}_{-10.32}$
246.00	248.00	$1.43^{+0.28}_{-0.17}$	$1.71^{+0.15}_{-0.42}$	$5.21^{+0.01}_{-0.19}$	$1.66^{+0.36}_{-0.01}$	$4.34^{+0.24}_{-0.24}$	$7.05^{+1.82}_{-2.32}$	$4.52^{+2.38}_{-2.63}$	$15.26^{+0.52}_{-0.15}$	$55.03^{+0.47}_{-1.91}$	153.13/128.00	$507.62^{+26.82}_{-19.89}$
248.00	250.00	$1.73^{+0.14}_{-0.44}$	$1.69^{+0.15}_{-0.39}$	$5.02^{+0.18}_{-0.08}$	$2.08^{+0.07}_{-0.44}$	$3.51^{+0.24}_{-0.20}$	$7.25^{+1.30}_{-4.16}$	$1.82^{+3.20}_{-0.59}$	$15.38^{+0.34}_{-0.73}$	$48.53^{+2.48}_{-0.76}$	132.36/128.00	$398.58^{+33.46}_{-12.65}$
250.00	252.00	$1.85^{+0.24}_{-0.37}$	$1.32^{+0.49}_{-0.06}$	$5.04^{+0.04}_{-0.14}$	$1.81^{+0.37}_{-0.05}$	$4.42^{+0.38}_{-0.20}$	$7.15^{+1.55}_{-3.11}$	$3.39^{+0.31}_{-2.38}$	$15.00^{+0.80}_{-0.13}$	$53.67^{+1.80}_{-1.28}$	151.41/128.00	$420.27^{+29.03}_{-17.07}$
252.00	254.00	$1.75^{+0.03}_{-0.40}$	$1.46^{+0.32}_{-0.30}$	$5.03^{+0.17}_{-0.06}$	$1.89^{+0.09}_{-0.28}$	$4.16^{+0.29}_{-0.34}$	$7.54^{+0.64}_{-4.09}$	$4.92^{+3.13}_{-2.73}$	$15.37^{+0.47}_{-0.24}$	$52.09^{+2.88}_{-0.70}$	114.79/128.00	$420.27^{+29.03}_{-17.07}$
254.00	256.00	$1.61^{+0.01}_{-0.41}$	$1.90^{+0.03}_{-0.34}$	$5.38^{+0.02}_{-0.16}$	$2.01^{+0.18}_{-0.22}$	$4.13^{+0.24}_{-0.13}$	$7.46^{+1.46}_{-2.48}$	$0.66^{+1.98}_{-0.08}$	$15.00^{+0.60}_{-0.35}$	$53.82^{+1.16}_{-1.19}$	194.01/128.00	$543.94^{+16.53}_{-13.61}$
256.00	257.00	$1.69^{+0.37}_{-0.31}$	$1.55^{+0.36}_{-0.10}$	$5.38^{+0.18}_{-0.03}$	$2.30^{+0.09}_{-0.56}$	$3.49^{+0.27}_{-0.04}$	$5.82^{+2.79}_{-1.46}$	$0.37^{+0.93}_{-0.13}$	$15.05^{+0.44}_{-0.99}$	$49.83^{+2.70}_{-0.33}$	199.43/128.00	$747.44^{+22.72}_{-23.76}$
257.00	258.00	$1.75^{+0.44}_{-0.49}$	$1.58^{+0.27}_{-0.13}$	$5.37^{+0.20}_{-0.17}$	$2.39^{+0.16}_{-0.57}$	$3.15^{+0.11}_{-0.09}$	$5.77^{+2.50}_{-1.66}$	$2.53^{+2.31}_{-0.05}$	$15.01^{+0.39}_{-0.94}$	$45.85^{+2.70}_{-3.58}$	256.85/128.00	$747.44^{+22.72}_{-23.76}$
258.00	259.00	$1.41^{+0.53}_{-0.12}$	$1.59^{+0.28}_{-0.10}$	$5.51^{+0.36}_{-0.17}$	$2.46^{+0.08}_{-0.68}$	$3.40^{+0.12}_{-0.04}$	$5.31^{+2.46}_{-1.22}$	$8.04^{+0.80}_{-1.29}$	$15.09^{+0.19}_{-1.33}$	$41.43^{+4.35}_{-1.19}$	312.69/128.00	[683.23, 725.39]
259.00	260.00	$1.46^{+0.35}_{-0.26}$	$1.42^{+0.38}_{-0.07}$	$5.55^{+0.31}_{-0.02}$	$2.09^{+0.23}_{-0.38}$	$3.90^{+0.09}_{-0.08}$	$6.41^{+2.71}_{-0.33}$	$6.24^{+0.39}_{-1.63}$	$14.51^{+0.47}_{-0.77}$	$47.69^{+3.56}_{-1.12}$	271.69/128.00	$640.56^{+22.52}_{-1.47}$
260.00	261.00	$1.35^{+0.43}_{-0.17}$	$1.54^{+0.18}_{-0.23}$	$5.36^{+0.00}_{-0.02}$	$2.82^{+0.07}_{-0.24}$	$3.80^{+0.04}_{-0.04}$	$5.62^{+2.34}_{-1.04}$	$9.60^{+0.04}_{-1.49}$	$15.77^{+0.09}_{-0.51}$	$39.93^{+2.18}_{-1.06}$	328.50/128.00	[477.02, 490.39]
261.00	262.00	$1.44^{+0.43}_{-0.21}$	$1.78^{+0.08}_{-0.32}$	$5.78^{+0.04}_{-0.25}$	$1.91^{+0.49}_{-0.18}$	$3.93^{+0.08}_{-0.16}$	$5.93^{+2.66}_{-1.33}$	$1.66^{+0.92}_{-0.25}$	$14.39^{+0.89}_{-0.43}$	$54.09^{+0.44}_{-3.19}$	299.94/128.00	$1073.02^{+35.16}_{-7.39}$
262.00	263.00	$2.12^{+0.25}_{-0.67}$	$1.75^{+0.06}_{-0.36}$	$5.76^{+0.12}_{-0.14}$	$1.89^{+0.25}_{-0.24}$	$3.84^{+0.05}_{-0.16}$	$6.07^{+2.85}_{-0.70}$	$2.32^{+1.32}_{-0.47}$	$13.88^{+0.65}_{-0.46}$	$52.28^{+1.36}_{-2.34}$	365.89/128.00	$930.24^{+30.48}_{-4.27}$
263.00	264.00	$1.49^{+0.17}_{-0.29}$	$1.64^{+0.21}_{-0.25}$	$5.55^{+0.16}_{-0.05}$	$2.17^{+0.16}_{-0.49}$	$3.74^{+0.10}_{-0.15}$	$5.12^{+3.58}_{-0.09}$	$2.60^{+2.57}_{-0.28}$	$14.86^{+0.36}_{-0.63}$	$50.89^{+1.51}_{-1.56}$	268.71/128.00	$1063.18^{+37.37}_{-7.32}$
264.00	266.00	$1.83^{+0.71}_{-0.11}$	$1.73^{+0.11}_{-0.29}$	$5.39^{+0.15}_{-0.02}$	$2.43^{+0.14}_{-0.51}$	$3.64^{+0.05}_{-0.08}$	$5.24^{+3.24}_{-0.61}$	$1.43^{+0.72}_{-0.16}$	$15.11^{+0.26}_{-1.16}$	$49.77^{+1.00}_{-1.25}$	311.02/128.00	$1063.18^{+37.37}_{-7.32}$
266.00	268.00	$1.83^{+0.85}_{-0.02}$	$1.66^{+0.22}_{-0.18}$	$5.21^{+0.17}_{-0.02}$	$2.47^{+0.12}_{-0.54}$	$3.73^{+0.13}_{-0.06}$	$5.40^{+3.51}_{-0.28}$	$0.20^{+0.69}_{-0.03}$	$15.34^{+0.25}_{-1.28}$	$50.42^{+1.92}_{-0.72}$	177.88/128.00	$459.76^{+19.46}_{-3.17}$
268.00	270.00	$1.44^{+0.18}_{-0.20}$	$1.43^{+0.46}_{-0.03}$	$5.22^{+0.17}_{-0.05}$	$2.20^{+0.01}_{-0.53}$	$3.90^{+0.36}_{-0.23}$	$6.07^{+1.89}_{-2.83}$	$1.26^{+2.84}_{-0.19}$	$15.49^{+0.15}_{-0.73}$	$51.33^{+2.85}_{-0.70}$	220.05/128.00	$733.79^{+41.70}_{-13.40}$
270.00	272.00	$1.49^{+0.22}_{-0.23}$	$1.73^{+0.11}_{-0.45}$	$5.20^{+0.04}_{-0.19}$	$1.67^{+0.40}_{-0.04}$	$2.89^{+0.41}_{-0.02}$	$8.21^{+0.29}_{-4.54}$	$4.44^{+2.04}_{-2.25}$	$15.06^{+0.63}_{-0.22}$	$46.78^{+2.04}_{-0.92}$	147.27/128.00	[606.12, 675.41]

Table B1
(Continued)

$t1$ (s)	$t2$ (s)	log (B_0) (G)	α_B	logγ_{min}	logΓ	p	t_{inj} (s)	q	log (R_0) (cm)	log (Q_0) (s^{-1})	PGSTAT/dof	E_p (keV)
500.00	502.00	$1.71^{+0.75}_{-0.03}$	$1.49^{+0.29}_{-0.32}$	$4.87^{+0.04}_{-0.34}$	$1.71^{+0.20}_{-0.14}$	$3.65^{+0.75}_{-0.11}$	$4.00^{+4.18}_{-1.53}$	$3.06^{+3.50}_{-1.55}$	$15.48^{+0.35}_{-0.26}$	$50.64^{+3.34}_{-1.36}$	174.23/128.00	$307.96^{+54.71}_{-3.53}$
502.00	504.00	$1.58^{+0.70}_{-0.06}$	$1.70^{+0.05}_{-0.48}$	$4.85^{+0.12}_{-0.16}$	$1.97^{+0.14}_{-0.29}$	$4.09^{+0.52}_{-0.17}$	$5.47^{+2.72}_{-1.98}$	$3.19^{+3.20}_{-1.60}$	$15.65^{+0.04}_{-0.74}$	$51.74^{+2.45}_{-1.64}$	142.02/128.00	$255.55^{+17.02}_{-20.87}$
504.00	506.00	$2.38^{+0.27}_{-0.50}$	$1.80^{+0.04}_{-0.58}$	$4.52^{+0.25}_{-0.10}$	$1.60^{+0.25}_{-0.04}$	$2.40^{+0.45}_{-0.07}$	$6.72^{+0.80}_{-3.66}$	$5.17^{+1.47}_{-3.81}$	$15.70^{+0.14}_{-0.48}$	$44.37^{+1.87}_{-0.98}$	158.14/128.00	$505.29^{+46.52}_{-53.92}$
506.00	508.00	$1.69^{+0.29}_{-0.32}$	$1.43^{+0.35}_{-0.23}$	$4.82^{+0.20}_{-0.08}$	$2.18^{+0.07}_{-0.42}$	$4.89^{+0.02}_{-0.58}$	$3.04^{+3.22}_{-0.62}$	$2.35^{+4.01}_{-0.37}$	$15.61^{+0.23}_{-0.42}$	$54.98^{+0.45}_{-2.28}$	155.73/128.00	$323.97^{+6.02}_{-29.19}$
508.00	510.00	$1.13^{+0.29}_{-0.03}$	$1.34^{+0.48}_{-0.07}$	$5.17^{+0.00}_{-0.24}$	$1.71^{+0.38}_{-0.09}$	$2.97^{+0.16}_{-0.07}$	$6.55^{+1.21}_{-3.32}$	$2.16^{+4.83}_{-0.38}$	$15.03^{+0.70}_{-0.17}$	$47.41^{+0.52}_{-1.72}$	169.79/128.00	$339.24^{+17.63}_{-26.27}$
510.00	511.00	$1.17^{+0.77}_{-0.04}$	$1.39^{+0.44}_{-0.13}$	$5.17^{+0.05}_{-0.11}$	$1.81^{+0.29}_{-0.15}$	$3.07^{+0.11}_{-0.06}$	$6.75^{+1.69}_{-2.52}$	$6.13^{+0.48}_{-3.13}$	$15.08^{+0.23}_{-0.69}$	$46.93^{+0.83}_{-2.09}$	158.93/128.00	$407.87^{+5.68}_{-33.32}$
511.00	512.00	$1.99^{+0.57}_{-0.61}$	$1.24^{+0.55}_{-0.01}$	$5.19^{+0.16}_{-0.15}$	$2.20^{+0.23}_{-0.52}$	$3.55^{+0.29}_{-0.06}$	$6.51^{+1.96}_{-2.65}$	$0.67^{+4.86}_{-0.02}$	$14.65^{+0.74}_{-0.58}$	$49.18^{+2.19}_{-1.19}$	147.35/128.00	$443.13^{+31.70}_{-15.05}$
512.00	514.00	$1.86^{+0.06}_{-0.54}$	$1.47^{+0.33}_{-0.21}$	$5.02^{+0.16}_{-0.07}$	$1.81^{+0.24}_{-0.17}$	$3.22^{+0.22}_{-0.14}$	$4.82^{+1.83}_{-2.09}$	$5.53^{+1.46}_{-2.82}$	$14.73^{+0.76}_{-0.20}$	$46.43^{+2.75}_{-0.24}$	131.44/128.00	$447.23^{+21.08}_{-27.93}$
514.00	516.00	$1.44^{+0.20}_{-0.20}$	$1.48^{+0.32}_{-0.28}$	$5.00^{+0.14}_{-0.11}$	$1.86^{+0.17}_{-0.26}$	$2.19^{+0.28}_{-0.03}$	$7.01^{+1.29}_{-3.48}$	$4.97^{+2.29}_{-2.61}$	$15.46^{+0.33}_{-0.37}$	$41.72^{+2.56}_{-0.10}$	180.11/128.00	$848.37^{+121.24}_{-129.63}$
516.00	518.00	$1.67^{+0.37}_{-0.28}$	$1.50^{+0.34}_{-0.26}$	$5.04^{+0.13}_{-0.16}$	$1.77^{+0.34}_{-0.10}$	$2.99^{+0.74}_{-0.27}$	$4.21^{+3.84}_{-0.91}$	$5.13^{+0.78}_{-3.07}$	$15.15^{+0.59}_{-0.12}$	$46.59^{+4.01}_{-2.38}$	140.25/128.00	$643.52^{+110.84}_{-28.97}$
518.00	520.00	$1.42^{+0.49}_{-0.05}$	$1.30^{+0.39}_{-0.15}$	$4.96^{+0.06}_{-0.15}$	$1.78^{+0.19}_{-0.17}$	$2.42^{+0.29}_{-0.13}$	$6.77^{+1.53}_{-3.47}$	$5.19^{+1.01}_{-3.45}$	$15.46^{+0.28}_{-0.52}$	$43.46^{+2.02}_{-1.04}$	168.44/128.00	$481.43^{+134.53}_{-13.12}$

Note. All errors represent the 1σ uncertainties.

ORCID iDs

Jun Yang https://orcid.org/0000-0002-5485-5042
Xiao-Hong Zhao https://orcid.org/0000-0003-3659-4800
Zhenyu Yan https://orcid.org/0009-0008-2841-3065
Xiangyu Ivy Wang https://orcid.org/0000-0002-9738-1238
Ce Cai https://orcid.org/0000-0002-6540-2372
Xiang Ma https://orcid.org/0000-0002-2032-2440
Yan-Zhi Meng https://orcid.org/0000-0002-1122-1146
Li-Ming Song https://orcid.org/0000-0003-0274-3396
Ping Wang https://orcid.org/0000-0003-0466-2223
Shuo Xiao https://orcid.org/0000-0003-2957-2806
Yu-Han Yang https://orcid.org/0000-0003-0691-6688
Yi-Han Iris Yin https://orcid.org/0000-0002-5596-5059
Bing Zhang https://orcid.org/0000-0002-9725-2524
Shuai Zhang https://orcid.org/0000-0002-4799-0780
Shuang-Nan Zhang https://orcid.org/0000-0001-5586-1017
Shao-Lin Xiong https://orcid.org/0000-0002-4771-7653
Bin-Bin Zhang https://orcid.org/0000-0003-4111-5958

References

Akaike, H. 1974, ITAC, 19, 716
Alves Batista, R. 2022, arXiv:2210.12855
Amati, L., Frontera, F., Tavani, M., et al. 2002, A&A, 390, 81
An, Z.-H., Antier, S., Bi, X.-Z., et al. 2023, arXiv:2303.01203
Arnaud, K. A. 1996, in ASP Conf. Ser. 101, Astronomical Data Analysis Software and Systems V, ed. G. H. Jacoby & J. Barnes (San Francisco, CA: ASP), 17
Band, D., Matteson, J., Ford, L., et al. 1993, ApJ, 413, 281
Beloborodov, A. M. 2010, MNRAS, 407, 1033
Berlato, F., Greiner, J., & Burgess, J. M. 2019, ApJ, 873, 60
Buchner, J., Georgakakis, A., Nandra, K., et al. 2014, A&A, 564, A125
Burgess, J. M., Bégué, D., Greiner, J., et al. 2020, NatAs, 4, 174
Burgess, J. M., Preece, R. D., Connaughton, V., et al. 2014, ApJ, 784, 17
Burgess, J. M., Yu, H.-F., Greiner, J., & Mortlock, D. J. 2018, MNRAS, 476, 1427
Castro-Tirado, A. J., Sanchez-Ramirez, R., Hu, Y. D., et al. 2022, GCN, 32686, 1
Daigne, F., Bošnjak, Ž, & Dubus, G. 2011, A&A, 526, A110
Daigne, F., & Mochkovitch, R. 1998, MNRAS, 296, 275
Feroz, F., & Hobson, M. P. 2008, MNRAS, 384, 449
Feroz, F., Hobson, M. P., & Bridges, M. 2009, MNRAS, 398, 1601
Feroz, F., Hobson, M. P., Cameron, E., & Pettitt, A. N. 2019, OJAp, 2, 10
Frederiks, D., Svinkin, D., Lysenko, A. L., et al. 2023, arXiv:2302.13383
Ghisellini, G., Celotti, A., & Lazzati, D. 2000, MNRAS, 313, L1
Huang, Y., Hu, S., Chen, S., et al. 2022, GCN, 32677, 1
Kaneko, Y., Preece, R. D., Briggs, M. S., et al. 2006, ApJS, 166, 298
Krishak, A., & Desai, S. 2020, JCAP, 2020, 006
Kumar, P., & Zhang, B. 2015, PhR, 561, 1
Lazzati, D., & Begelman, M. C. 2010, ApJ, 725, 1137
Lesage, S., Veres, P., Roberts, O. J., et al. 2022, GCN, 32642, 1
Liu, J. C., Zhang, Y. Q., Xiong, S. L., et al. 2022, GCN, 32751, 1
Malesani, D. B., Levan, A. J., Izzo, L., et al. 2023, arXiv:2302.07891
Meegan, C., Lichti, G., Bhat, P. N., et al. 2009, ApJ, 702, 791
Mészáros, P., & Rees, M. J. 2000, ApJ, 530, 292
Minaev, P. Y., & Pozanenko, A. S. 2020, MNRAS, 492, 1919
Oganesyan, G., Nava, L., Ghirlanda, G., & Celotti, A. 2017, ApJ, 846, 137
Oganesyan, G., Nava, L., Ghirlanda, G., & Celotti, A. 2018, A&A, 616, A138
Oganesyan, G., Nava, L., Ghirlanda, G., Melandri, A., & Celotti, A. 2019, A&A, 628, A59
Planck Collaboration, Aghanim, N., Akrami, Y., et al. 2020, A&A, 641, A6
Preece, R. D., Briggs, M. S., Mallozzi, R. S., et al. 2000, ApJS, 126, 19
Ravasio, M. E., Ghirlanda, G., Nava, L., & Ghisellini, G. 2019, A&A, 625, A60
Ravasio, M. E., Oganesyan, G., Ghirlanda, G., et al. 2018, A&A, 613, A16
Rees, M. J., & Mészáros, P. 2005, ApJ, 628, 847
Ren, J., Wang, Y., & Zhang, L.-L. 2022, arXiv:2210.10673
Rudolph, A., Petropoulou, M., Winter, W., & Bošnjak, Ž 2023, ApJL, 944, L34
Rybicki, G. B., & Lightman, A. P. 1979, Radiative Processes in Astrophysics (New York: Wiley)
Sari, R. 1998, ApJL, 494, L49
Sato, Y., Murase, K., Ohira, Y., & Yamazaki, R. 2023, MNRAS, Advance Access
Scargle, J. D., Norris, J. P., Jackson, B., & Chiang, J. 2013, ApJ, 764, 167
Shao, X., & Gao, H. 2022, ApJ, 927, 173
Spruit, H. C., Daigne, F., & Drenkhahn, G. 2001, A&A, 369, 694
Sugiura, N. 1978, Communications in Statistics-theory and Methods, 7, 13
Uhm, Z. L., & Zhang, B. 2014, NatPh, 10, 351
Veres, P., Burns, E., Bissaldi, E., et al. 2022, GCN, 32636, 1
Wang, D.-Z., Zhao, X.-H., Zhang, Z. J., Zhang, B.-B., & Peng, Z.-Y. 2022, ApJ, 926, 178
Wang, K., Ma, Z.-P., Liu, R.-Y., et al. 2023, arXiv:2302.11111
Yang, J., Ai, S., Zhang, B.-B., et al. 2022, Natur, 612, 232
Zhang, B. 2018, The Physics of Gamma-Ray Bursts (Cambridge: Cambridge Univ. Press)
Zhang, B. 2020, NatAs, 4, 210
Zhang, B., & Pe'er, A. 2009, ApJL, 700, L65
Zhang, B., & Yan, H. 2011, ApJ, 726, 90
Zhang, B., & Zhang, B. 2014, ApJ, 782, 92
Zhang, B., Zhang, B.-B., Virgili, F. J., et al. 2009, ApJ, 703, 1696
Zhang, B.-B., Uhm, Z. L., Connaughton, V., Briggs, M. S., & Zhang, B. 2016, ApJ, 816, 72
Zhang, B. B., Zhang, B., Castro-Tirado, A. J., et al. 2018, NatAs, 2, 69
Zhang, B.-B., Zhang, B., Liang, E.-W., et al. 2011, ApJ, 730, 141
Zhang, B. T., Murase, K., Ioka, K., et al. 2022, arXiv:2211.05754